Supporting Information

Time-Resolved Tracking of Hot Carrier Relaxation in Two Types of MBenes

Jie Zhao,[ab] Qi Zhang,[ab] Pan Xiong,[b] Chunli Wang,[c] Liangzhu Zhang,*[c] Jiebo Li,[d] Kun Zhao,*[a] Ruifeng Lu,[a] Kaijun Yuan,*[bef] and Xueming Yang[beg]*

[a]Department of Applied Physics, Nanjing University of Science and Technology, Nanjing 210094, China.

[b]State Key Laboratory of Chemical Reaction Dynamics, Dalian Institute of Chemical Physics, Chinese Academy of Sciences, Dalian 116023, China.

[c]School of Materials Science and Engineering, East China University of Science and Technology, Shanghai 200237, China.

[d]Institute of Medical Photonics, Beijing Advanced Innovation Center for Biomedical Engineering, School of Biological Science and Medical Engineering, Beihang University, Beijing 100191, China.

[e]Hefei National Laboratory, Hefei 230026, China.

[f]University of Chinese Academy of Sciences, Beijing 101408, China.

[g]Department of Chemistry and Center for Advanced Light Source Research, College of Science, Southern University of Science and Technology, Shenzhen 518055, China.

*Corresponding author. Email: zhangqi24@njust.edu.cn; zhaokun@njust.edu.cn; kjyuan@dicp.ac.cn; zhangliangzhu@ecust.edu.cn

Section S1. Sample preparation

Synthesis of MoB MBene. The MoAlB phase was synthesized by solid phase reaction. Mo, B and Al powders in a 1:1:1.6 molar ratio was ball-milled for 4 h. Then, the powder was sintered at 1100°C for 1 h in a tube furnace in an Ar gas. The powder was then washed with a 1 M hydrochloric acid (HCl) solution and stirred for 4 h to remove excess Al. After washing four times with deionized (DI) water, the MoAlB powder was collected and dried. This MoAlB phase served as a precursor for synthesizing MoB MBene nanosheets. MoB MBene nanosheets were synthesized by selectively removing the Al layer of MoAlB using a Lewis acid molten salt. The molar ratio of MoAlB, $ZnCl_2$, KCl, and LiCl was 1:10:4:4, and the mixture was loaded in an alumina boat. It was sintered at 700°C in an Ar gas in a tube furnace for 10 h. To remove soluble salts (i.e., $ZnCl_2$, KCl, and LiCl), the mixture was collected in DI water. Then, it is dispersed in a 1 M HCl solution and stirred for 4 h to eliminate Zn nanoparticles. Finally, the product is washed four times with DI water to obtain a solution of MoB MBene nanosheets.

Synthesis of $Mo_{4/3}B_{2-x}T_z$ MBene. Few-layer $Mo_{4/3}B_{2-x}T_z$ was purchased from Shandong Xiyan New Material Technology Co., Ltd. Hydrogen fluoride (HF; 20 mL, 40 wt.%) was added to 2 g of $(Mo_{2/3}Y_{1/3})_2AlB_2$, and the mixture was stirred in an oil bath for 210 min (temperature = 33°C). After etching, the sample was washed several times with degassed DI water (3500 rpm, 5 min each) until it was neutral, followed by centrifugation (5000 rpm, 1 min) to remove residual water, which finally afforded multilayer $Mo_{4/3}B_{2-x}T_z$. Then, 10 mL of tetrabutylammonium hydroxide (TBAOH; 20 wt.%) was added to multilayer MBene and shaken for 2 min. Then, the sample was washed with ethanol and centrifuged (6000 rpm, 2 min) three times to remove TBAOH. Then, it was washed three times with degassed DI water (6000 rpm, 2 min). Finally, 15 mL of DI water was added and gently shaken for 10 min to obtain single-layer $Mo_{4/3}B_{2-x}T_z$.

Section S2. ICP characterization of MoB MBene

The inductively coupled plasma optical emission spectroscopy (ICP-OES) analysis of the sample was performed using the PerkinElmer apparatus Optima 7300 DV instrument. On the Anton Paar Multiwave 3000 microwave digestion system, solid powder samples are digested using aqua regia and hydrogen peroxide, followed by the addition of an appropriate amount of water and dilution to a certain volume. The concentration of metals such as Mo is determined in ICP-OES mode and converted to mass content on the solid catalyst.

Section S3. Transient absorption spectroscopy measurement

Pump-probe measurements were performed using an amplified Ti: sapphire laser system (coherent Vitesse) equipped with an optical parametric amplifier (Coherent Legend Elite He + USP-1K-III). The output pulse (800 nm, 35 fs at 7 mJ with a bandwidth of 40 nm and a repetition rate of 1 kHz.) was split to generate pump and probe beams. A 240–2500 nm pump pulse was generated using an optical parametric amplifier. The probe pulse was focused onto a sapphire plate to produce a continuous white-light pulse (450–1100 nm). The temporal behavior was monitored by the delay stage (ALS10045-S-M-10-MT-LT45AS-CM, Aerotech) and was used to control the path length of the probe pulse and overlaps in time and space with the pump pulse. The probe beam was recorded using a fiber spectrometer (AvaSpec-ULS2048CLEVO, Avantes). A vacuum detection system, comprising a vacuum cell (Optistat DN-V, Oxford Instruments) and a vacuum pump (Duo 3, Pfeiffer Vacuum), was employed to measure all samples.

Section S4. Calculation details

The calculations of MoB (Figures 2g, 4ef, 5ab) are conducted within the framework of density functional theory using the projector augmented plane-wave method, as implemented in the Vienna ab initio simulation package.[1] The generalized gradient approximation proposed by Perdew, Burke, and Ernzerhof is chosen for the exchange-correlation potential.[2] The cutoff energy for the plane wave is set to 500 eV. The energy criterion is established at 10^{-10} eV for the iterative solution of the Kohn-Sham equation and 10^{-8} eV for atomic vibration calculations. Brillouin zone integration is performed using a 5x5x5 k-mesh. All structures are relaxed until the residual forces on the atoms decrease to less than 0.03 eV/Å. Phonon properties are calculated using Density Functional Perturbation Theory (DFPT), as implemented in VASP and PHONOPY software

packages, with a 2x1x2 supercell applied.[3] The $Mo_{4/3}B_2O_2$ structural model was adopted from "Broadband Nonlinear Response and Ultrafast Photonics Applications in Few-Layer MBene", and we acknowledge the authors for kindly providing the optimized structural information.[4]

Electron-phonon coupling (EPC) calculations

The structural optimization, phonon dispersion, phonon density of states, and electron-phonon coupling (EPC) calculations for MoB, MoBO, and MoBF materials were performed within the framework of density functional theory (DFT), using norm-conserving pseudopotentials[5] as implemented in the QUANTUM-ESPRESSO (QE) package[6]. The plane-wave kinetic energy cutoff and charge density cutoff were set to 80 Ry and 320 Ry, respectively, with a Methfessel-Paxton smearing width of 0.02 Ry. For the hexagonal (MoB and MoBO) and orthorhombic (MoBF) structures, Brillouin zone k-point grids of 8×8×1 and 4×8×1, respectively, were used for self-consistent electron density calculations. Corresponding q-point meshes (8×8×1 for hexagonal, 4×8×1 for orthorhombic) were employed to compute the dynamical matrices and EPC matrix elements. The phonon properties and EPC were calculated using density functional perturbation theory (DFPT)[7] and Eliashberg theory[8]. For MoBO and MoBF, the calculations of electronic band structures and density of states (DOS) were performed using density functional theory (DFT) as implemented in the Vienna Ab initio Simulation Package (VASP)[9]. The Perdew-Burke-Ernzerhof generalized gradient approximation (PBE-GGA)[10] was employed for the exchange-correlation functional, and the electron-ion interactions were described using the projector augmented wave (PAW)[11] method. The plane-wave cutoff energy was set to 600 eV, and Brillouin zone integration was carried out using Monkhorst-Pack k-point meshes of 12×12×1 for hexagonal structures and 8×12×1 for orthorhombic structures. The convergence criterion for the self-consistent electronic calculations was set to 1×10^{-6} eV.

Section S5. Global fitting for carrier dynamics

We performed global analysis of the carrier relaxation dynamics in MBenes using a multiexponential function:

$$\Delta A(\lambda, t) = IRF \otimes \sum_i [DAS_i(\lambda) \cdot \exp\left(^{-t}/_{\tau_i}\right)]$$

where ΔA (λ, t) is the transient absorption signal as a function of probe wavelength (λ) and delay time (t). IRF denotes the instrumental response function. DAS_i (λ) represents the decay-

associated difference spectrum for each component, which defines its amplitude at each wavelength. The term $\exp(-t/\tau_i)$ describes an exponential decay governed by the time constant τ_i of each component.[12, 13]

Section S6. Influence of Stoichiometry and Defects on Carrier Dynamics

It should be noted that, in addition to surface terminations, MoB and $Mo_{4/3}B_{2-x}T_z$ may also differ in stoichiometry and defect density. However, the influence of these factors on the e-p interaction stage investigated in this work can be considered negligible. First, differences in composition (stoichiometry) may lead to variations in the valence states of the constituent elements and further result in changes in the electronic density of states near the Fermi level, thereby influencing electron–phonon interactions[14, 15]. Since the electronic states near the Fermi level are mainly contributed by Mo atoms (Fig. 2g and Fig. S4), variations in the Mo oxidation state can affect the corresponding electronic structure. In MoB, Mo is predominantly in the +5 oxidation state, whereas in $Mo_{4/3}B_{2-x}T_z$ it mainly exists in mixed +5 and +6 states (Fig. 2e and Fig. S3c). The difference in Mo oxidation states between the two materials is relatively small and thus has a weak impact on the carrier dynamics. Second, with respect to defect density, a comparison between defect-poor $Mo_{4/3}B_{2-x}T_z$ and defect-rich $Mo_{4/3}B_{2-x}T_z$ (Fig. S18†), in which the defect density is significantly increased through oxidation treatment, reveals that their carrier dynamics within the first 2 ps remain essentially unchanged, suggesting that the influence of defect density on e–p interaction can be considered negligible.

Section S7. Effects of Surface Terminations on Electron–Phonon Scattering

According to previous studies, the e–p scattering time could be theoretically described based on Fermi's golden rule.[14, 15]

$$\frac{1}{\tau_\lambda^{ep}} = \frac{2\pi}{\hbar}\sum_{k,i,j} |g^\lambda_{jk+q,ik}|^2 \left(f_{ik} - f_{jk+q}\right)\delta\left(\epsilon_{ik} - \epsilon_{jk+q} + \hbar\omega_\lambda\right)$$

where τ_λ^{ep} is the e–p scattering time, g denotes the e–p coupling matrix element, f is the Fermi–Dirac distribution function, k represents the electron wave vector, i and j are the electronic band indices, ϵ denotes the electron energy, and ω is the phonon mode. Hence, the scattering time is determined by three factors: phonon modes, coupling constant, and DOS near the Fermi level.

Our results indicate that the increase in the number of vibrational phonon modes is the most critical factor.

The experimentally observed Raman linewidth changes (Fig. 4c, d) are consistent with the phonon modes obtained from the DFT phonon dispersion calculations (Fig. 4e, f), both indicating that the introduction of surface terminations leads to an increased number of vibrational phonon modes.

Experimentally, $Mo_{4/3}B_{2-x}T_z$ exhibits a larger Raman linewidth (101 cm^{-1}) than MoB (67 cm^{-1}). Quantitatively, the introduction of surface terminations increases the Raman linewidth by ~67%, indicating that additional vibrational modes are introduced, which provide extra channels for enhancing e–p scattering.

Our calculated electronic structure shows that the integrated DOS near the Fermi level in MoB (0.41, Fig. S24c) is about 14% higher than that in $Mo_{4/3}B_2T_z$ (0.36, Fig. S24d). As shown in Fig. S24, the integration window of 0.05 eV (~400 cm^{-1}) is selected according to the phonon energy range observed in Raman spectra (100–400 cm^{-1}). The results indicate that this factor plays a relatively minor role in decreasing e–p scattering.

In comparison, as shown in Fig. S17, the e–p coupling constant of MoB (0.406) is lower than those of terminated MoBF (0.445) and MoBO (0.510), with an average value of 0.480, representing an ~18% increase relative to MoB, increasing e–p scattering. Hence, this effect is still weaker than that arising from the increased number of vibrational phonon modes induced by surface terminations.

Based on the quantitative analysis of the above experimental and theoretical results, the increase in the number of vibrational phonon modes induced by surface terminations plays a dominant role in enhancing e–p interactions.

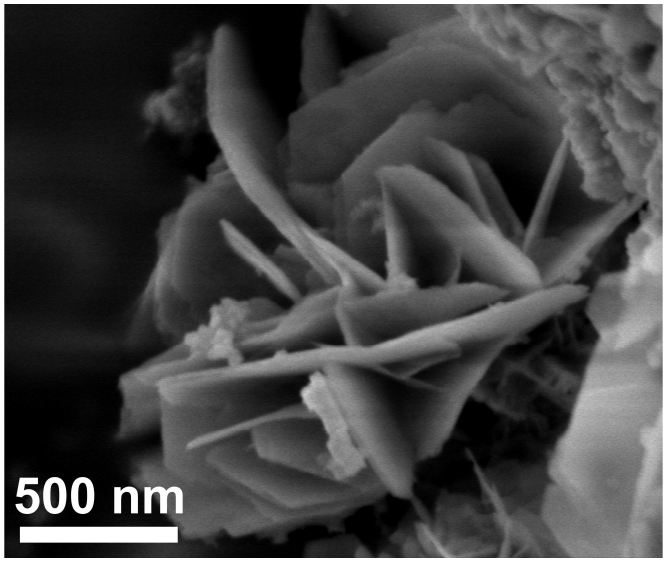

Figure S1. SEM image of MoB.

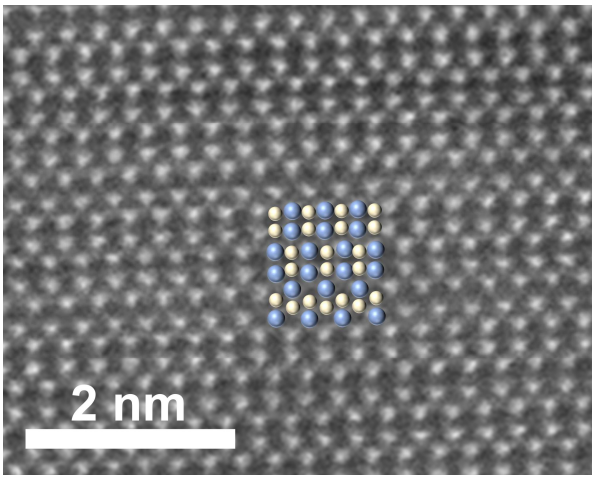

Figure S2. High-magnification STEM image of MoB MBene nanosheet. Blue spheres represent Mo atoms; B atoms, being much lighter, are not visible in the STEM image and are indicated by yellow spheres. The zigzag features shown in the image reflect the presence of stacking faults in MoB.

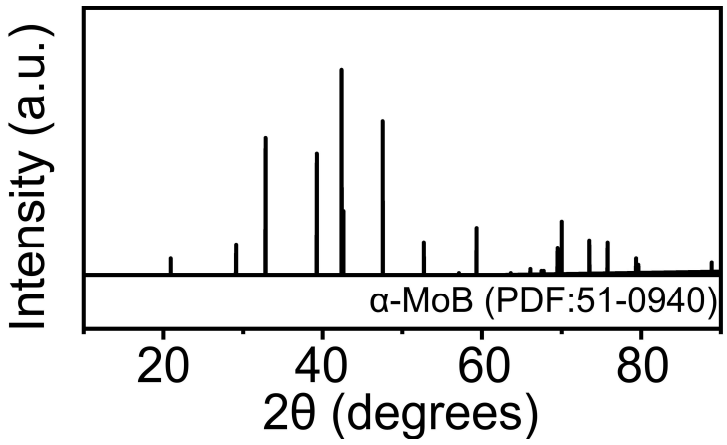

Figure S3. XRD patterns of α-MoB.

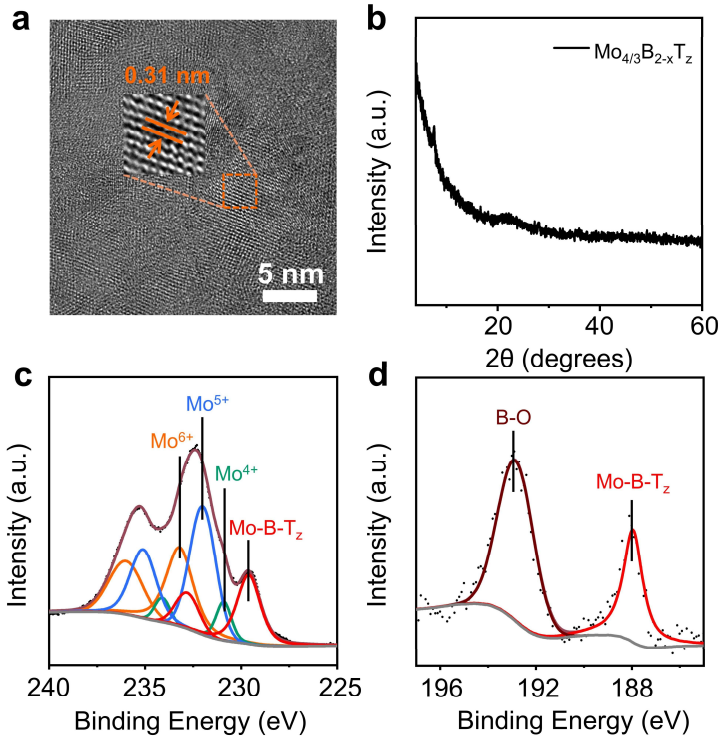

Figure S4. (a) High-resolution TEM image of $Mo_{4/3}B_{2-x}T_z$. (b) XRD pattern of $Mo_{4/3}B_{2-x}T_z$. (c, d) High-resolution XPS spectra of $Mo_{4/3}B_{2-x}T_z$ with peak fittings for the (c) Mo 3d and (d) B 1s regions.

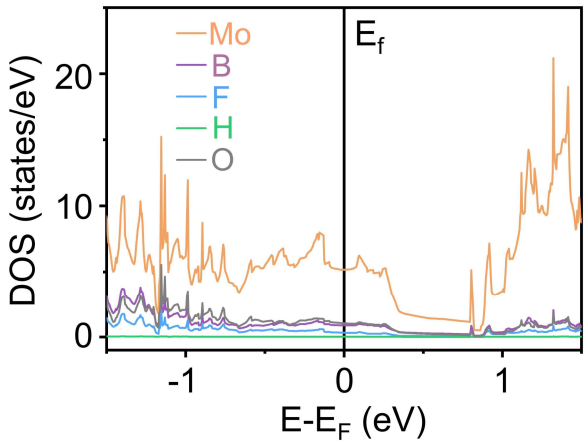

Figure S5. Partial DOS of $Mo_{4/3}B_2T_z$.

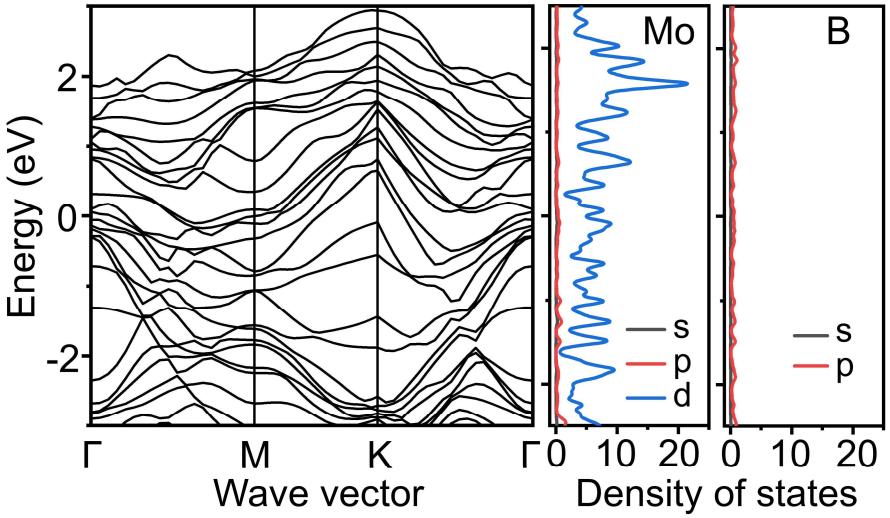

Figure S6. The calculated band structures and density of states of MoB.

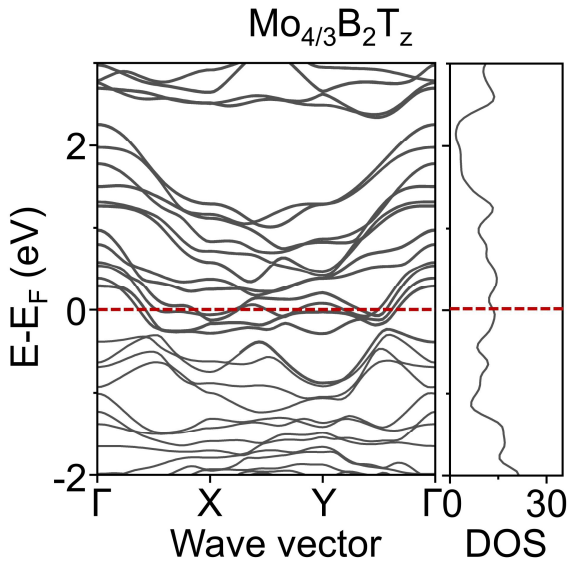

Figure S7. The calculated band structures and total density of states of $Mo_{4/3}B_2T_z$.

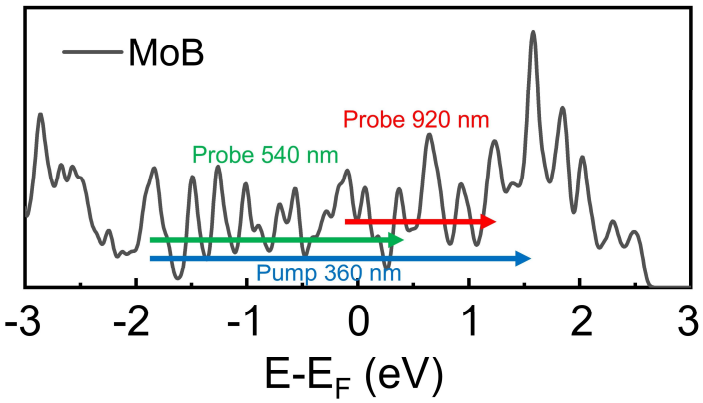

Figure S8. Total density of states (TDOS) of MoB.

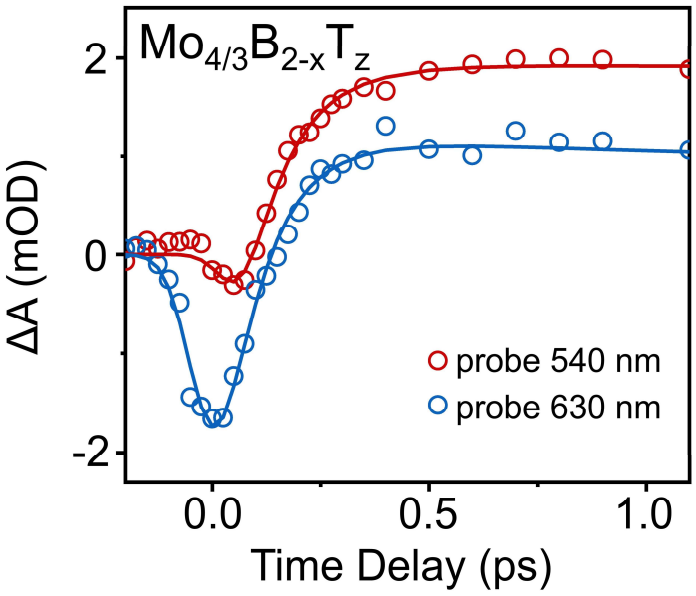

Figure S9. TA dynamic traces were probed at 540, and 630 nm, and the corresponding fitting results of $Mo_{4/3}B_{2-x}T_z$.

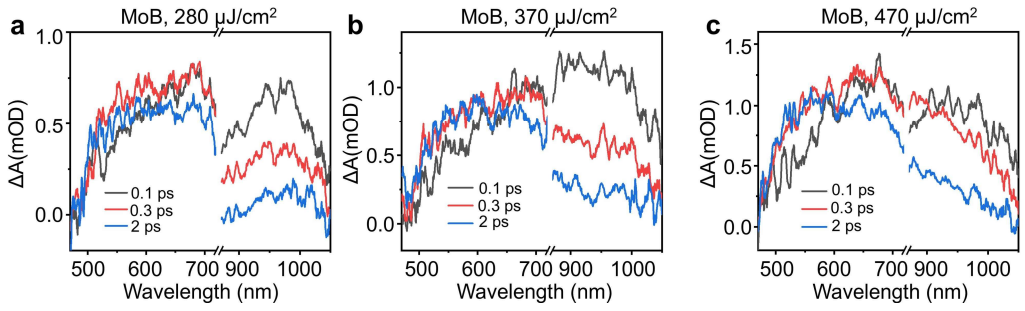

Figure S10. Transient absorption (TA) spectra of MoB at indicated delay time windows after excitation by a 360 nm pulse with the intensity of (a) 280 μJ/cm^2, (b) 370 μJ/cm^2 and (c) 470 μJ/cm^2.

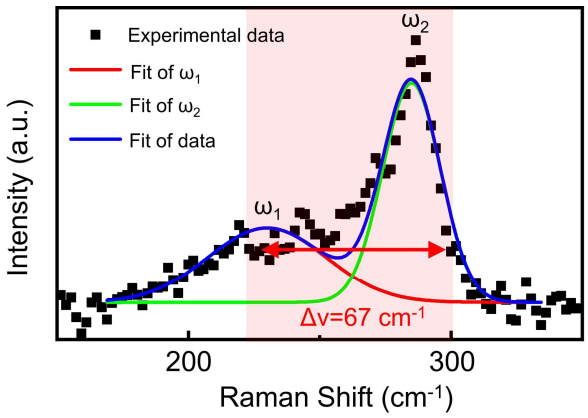

Figure S11. Raman spectrum of MoB excited with a 532 nm laser. The ω_1 and ω_2 modes exhibit full widths at half maximum of 45 and 22 cm^{-1}, respectively.

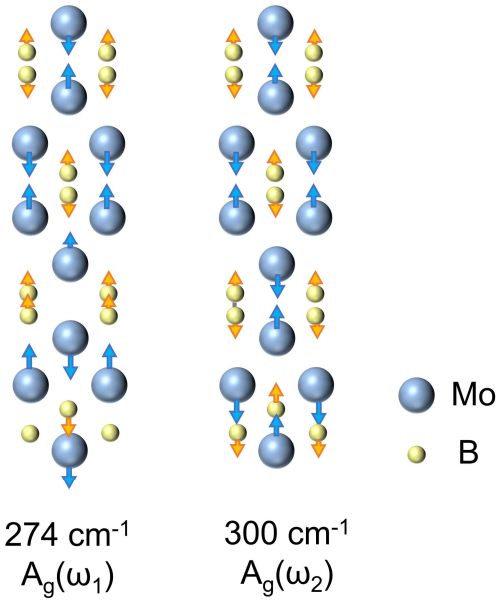

Figure S12. Schematic of the Raman active modes of MoB. The blue sphere represents Mo, the yellow represents B, and the arrows represent the vibration direction.

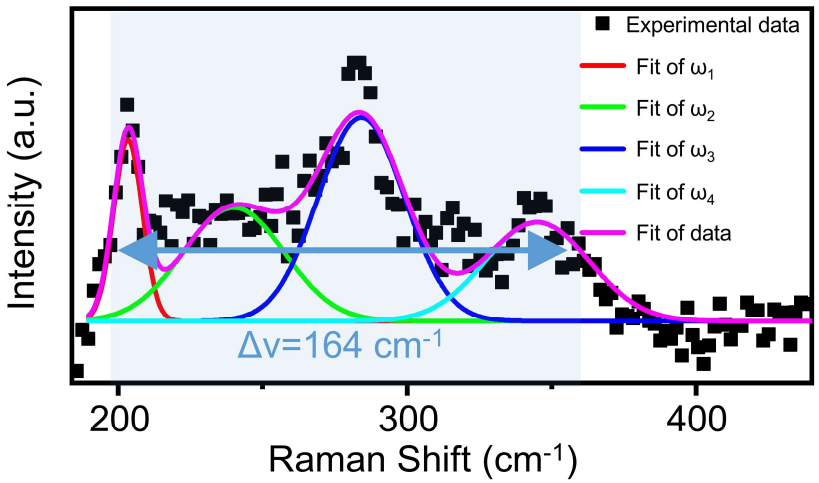

Figure S13. Raman spectra of the $Mo_{4/3}B_{2-x}T_z$ excited with the 532 nm laser. Four Raman peaks are resolved in the spectrum, located at 203, 240, 284, and 345 cm^{-1}. These peaks correspond to the E_{1g}, E_{1g}, A_{1g}, and E^1_{2g} vibrational modes, respectively.

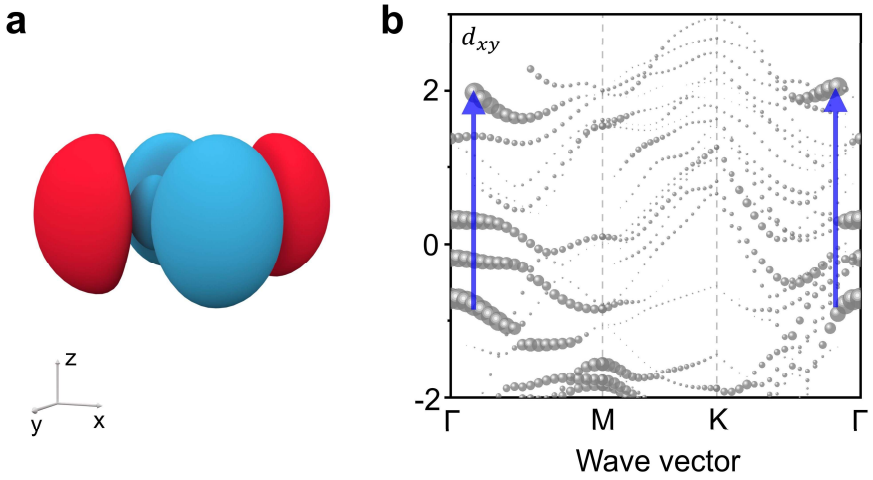

Figure S14. (a) Schematic diagram of the d_{xy} orbital. (b) The calculated fat band of the d_{xy} orbital of MoB. The diameters of the spheres represent the intensity of DOS. The blue arrows indicate possible electronic transitions after excitation.

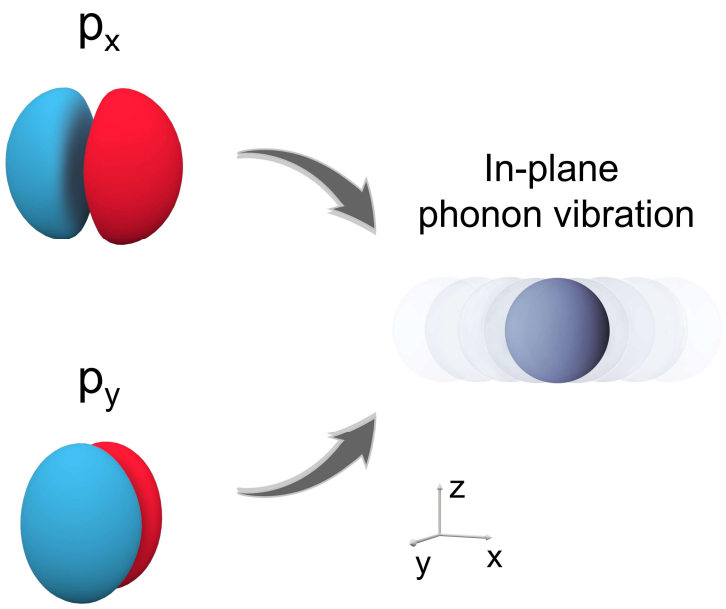

Figure S15. The coupling between the p_x and p_y electronic orbitals and phonons in graphene.

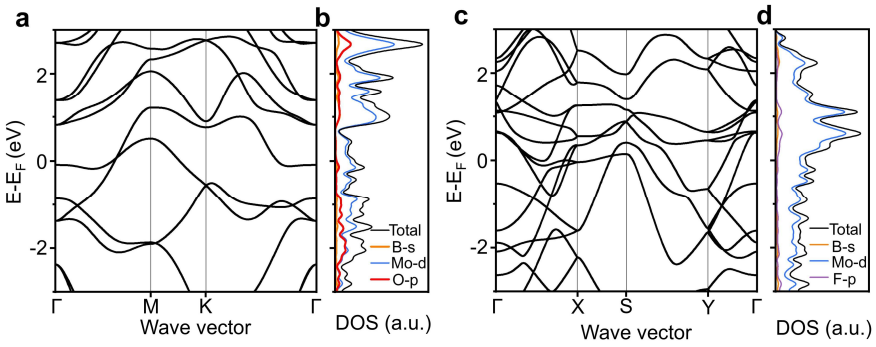

Figure S16. Orbital-resolved band structures and corresponding total and local DOSs of (a),(b) MoBO, (c),(d) MoBF.

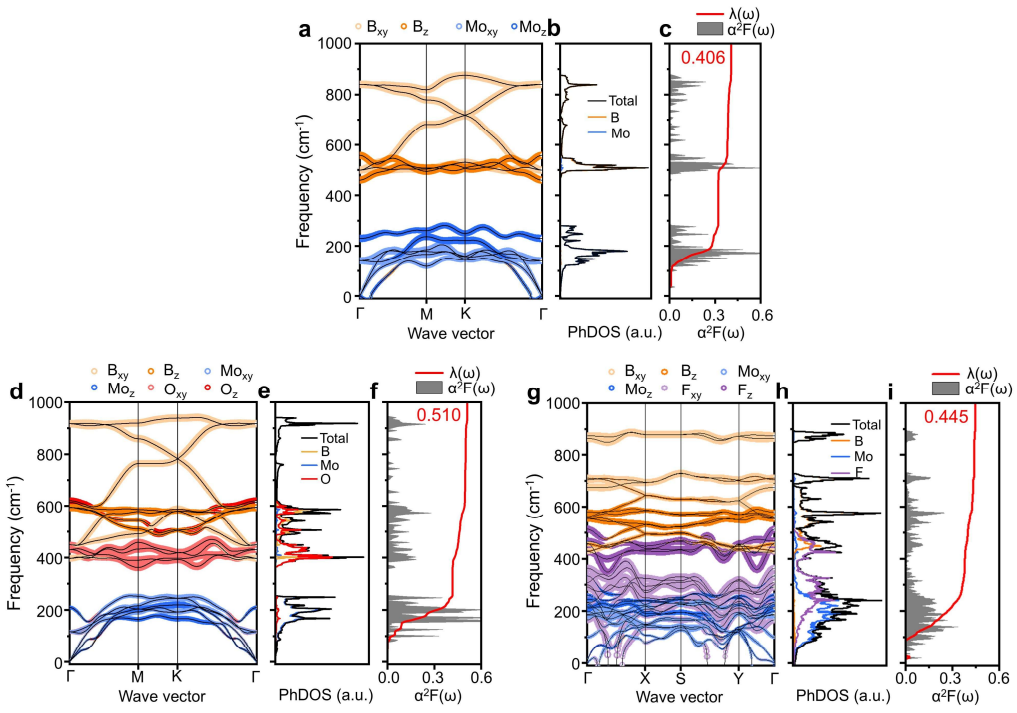

Figure S17. Phonon dispersions weighted by the motion modes of B, Mo, (T_x = O, F) atoms of (a) MoB, (d) MoBO and (g) MoBF. The light yellow, yellow, light blue, blue, light red, red, light purple, and purple hollow circles in (a), (d) and (g) represent B horizontal, B vertical, Mo horizontal, Mo vertical, O horizontal, O vertical, F horizontal, and F vertical modes, respectively. Phonon density of states (PhDOS) of (b) MoB, (e) MoBO and (h) MoBF. Eliashberg spectral function $\alpha^2F(\omega)$ and cumulative frequency dependence of EPC $\lambda(\omega)$ of (c) MoB, (f) MoBO and (i) MoBF.

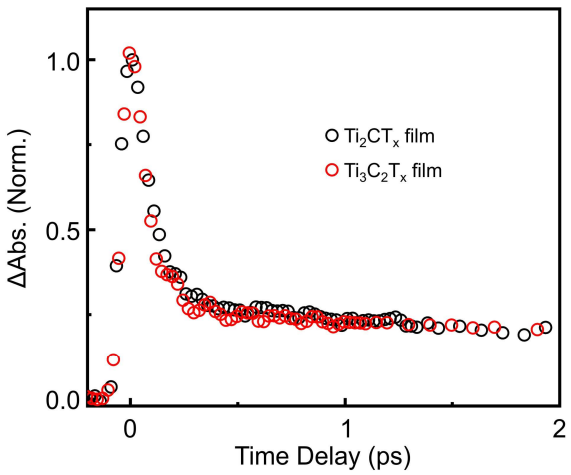

Figure S18. Normalized carrier dynamic curves of Ti_2CT_x film monitored at 585 nm wavelength after excitation at 920 nm and $Ti_3C_2T_x$ film monitored at 905 nm wavelength after excitation at 750 nm.

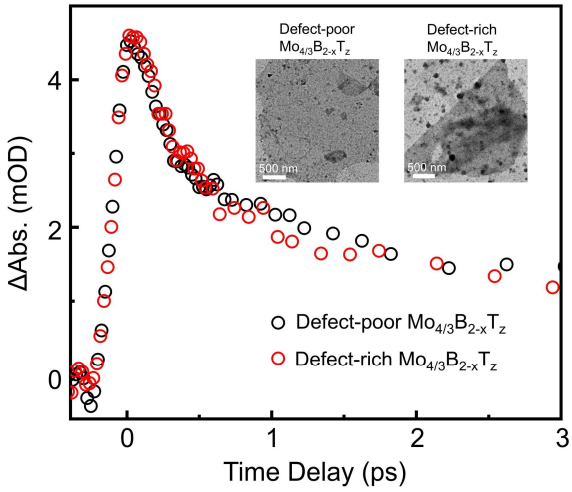

Figure S19. Normalized carrier dynamic curves of defect-poor $Mo_{4/3}B_{2-x}T_z$ and defect-rich $Mo_{4/3}B_{2-x}T_z$ monitored at 900 nm wavelength after excitation at 390 nm. Inset: Transmission electron microscopy (TEM) images of defect-poor $Mo_{4/3}B_{2-x}T_z$ and defect-rich $Mo_{4/3}B_{2-x}T_z$.

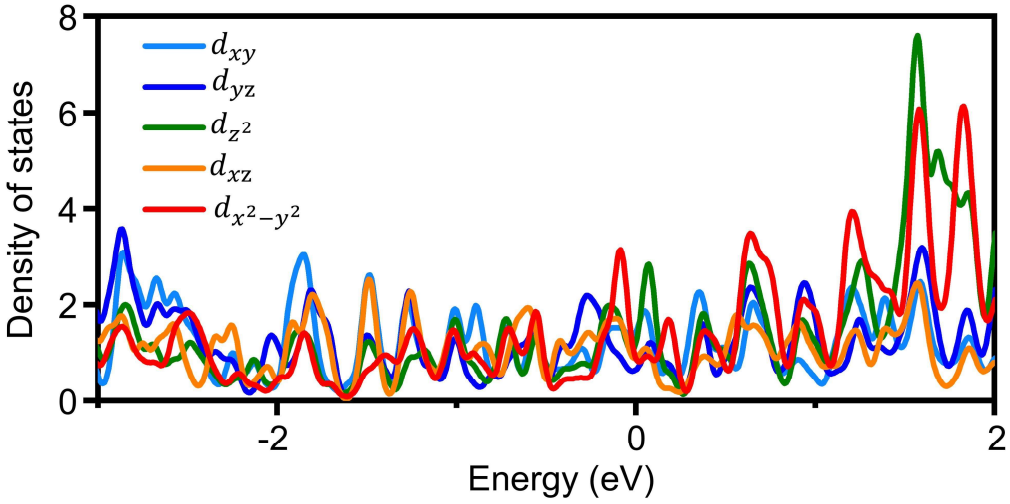

Figure S20. The DFT calculated the density of states (DOS) of d-electron orbitals in Mo within MoB.

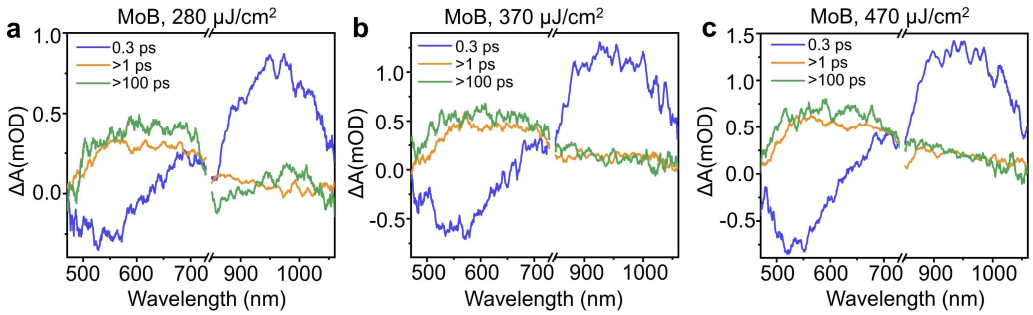

Figure S21. Decay-associated spectra (DAS) of MoB were obtained from global analysis of the TA data. (a-c) DAS for a pump pulse of (a) 280 μJ/cm^2, (b) 370 μJ/cm^2, and (c) 470 μJ/cm^2 energy density.

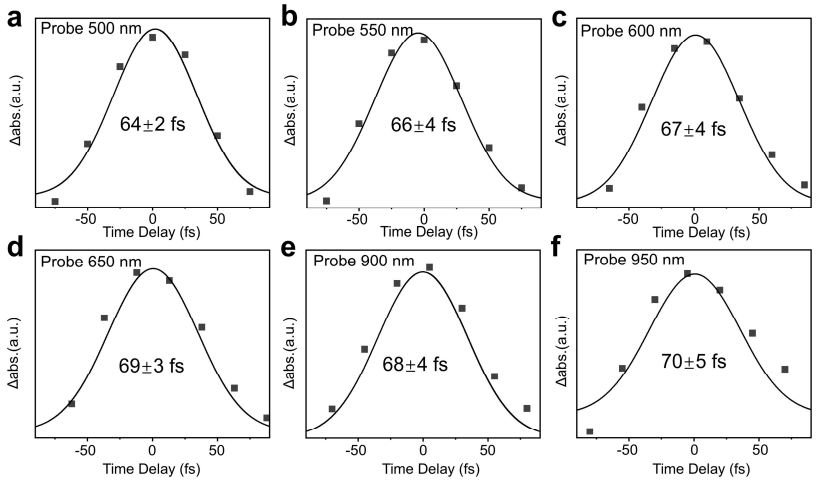

Figure S22. Pump–probe cross-correlation time measurements with the substrate (CaF_2) after excitation at 360 nm probed at (a) 500 nm, (b) 550 nm, (c) 600 nm, (d) 650 nm, (e) 900 nm and (f) 950 nm. The squares are experimental data and lines are fitted results with Gaussian function.

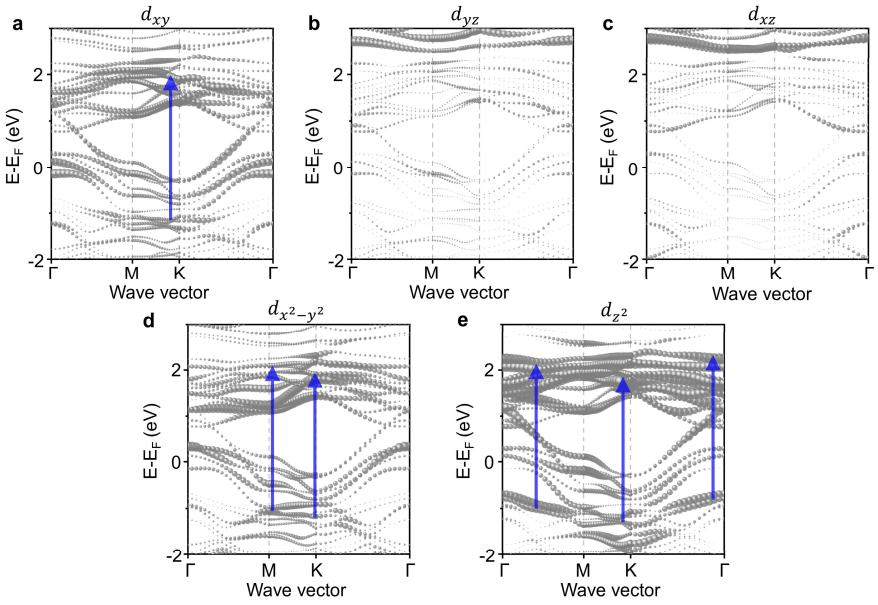

Figure S23. The calculated fat band of (a) d_{xy}, (b) d_{yz}, (c) d_{xz}, (d) $d_{x^2-y^2}$, (e) d_{z^2} of Mo in $Mo_{4/3}B_2T_z$. The diameters of the spheres represent the intensity of DOS. The blue arrows indicate possible electronic transitions after excitation.

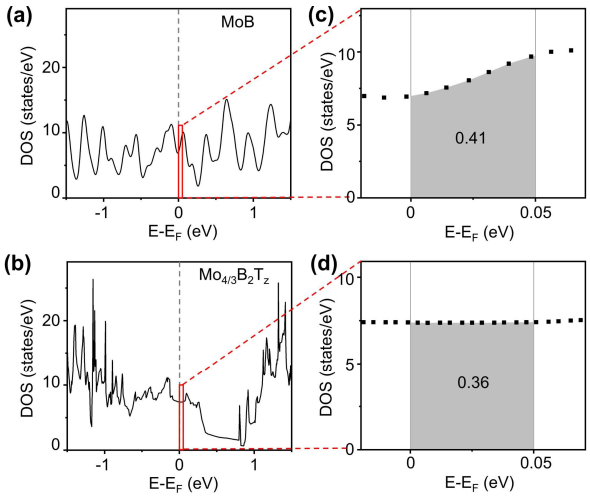

Figure S24. (a, b) TDOS of (a) MoB and (b) $Mo_{4/3}B_2T_z$. (c, d) Enlarged views of (a) MoB and (b) $Mo_{4/3}B_2T_z$.

References

1. G. Kresse and D. Joubert, *Physical Review B*, 1999, **59**, 1758.
2. J. P. Perdew, K. Burke and M. Ernzerhof, *Physical Review Letters*, 1996, **77**, 3865.
3. A. Togo, F. Oba and I. Tanaka, *Physical Review B*, 2008, **78**, 134106.
4. J. Guo, Y. Hao, A. V. Kuklin, W. Bao, S. Wageh, O. A. Al-Hartomy, A. G. Al-sehemi, H. Ågren, L. Gao and H. Zhang, *ACS Photonics*, 2023, **10**, 2353-2362.
5. M. Fuchs and M. Scheffler, *Computer Physics Communications*, 1999, **119**, 67-98.
6. P. Giannozzi, S. Baroni, N. Bonini, M. Calandra, R. Car, C. Cavazzoni, D. Ceresoli, G. L. Chiarotti, M. Cococcioni, I. Dabo, A. Dal Corso, S. de Gironcoli, S. Fabris, G. Fratesi, R. Gebauer, U. Gerstmann, C. Gougoussis, A. Kokalj, M. Lazzeri, L. Martin-Samos, N. Marzari, F. Mauri, R. Mazzarello, S. Paolini, A. Pasquarello, L. Paulatto, C. Sbraccia, S. Scandolo, G. Sclauzero, A. P. Seitsonen, A. Smogunov, P. Umari and R. M. Wentzcovitch, *Journal of physics. Condensed matter : an Institute of Physics journal*, 2009, **21**, 395502.
7. S. Baroni, S. de Gironcoli, A. Dal Corso and P. Giannozzi, *Reviews of Modern Physics*, 2001, **73**, 515-562.
8. P. B. Allen and B. Mitrović, *Solid State Physics*, 1983, **37**, 1-92.
9. G. Kresse and J. Furthmuller, *Physical Review B*, 1996, **54**, 11169-11186.
10. J. P. Perdew, K. Burke and M. Ernzerhof, *Physical Review Letters*, 1996, **77**, 3865-3868.
11. P. E. Blochl, *Physical Review B*, 1994, **50**, 17953-17979.
12. S. Schott, L. Ress, J. Hrušák, P. Nuernberger and T. Brixner, *Physical Chemistry Chemical Physics*, 2016, **18**, 33287-33302.
13. I. H. M. van Stokkum, D. S. Larsen and R. van Grondelle, *Biochimica et Biophysica Acta (BBA) - Bioenergetics*, 2004, **1657**, 82-104.

14. Y. Huang, J. Zhou, G. Wang and Z. Sun, *Journal of the American Chemical Society*, 2019, **141**, 8503-8508.
15. Z. Tong, S. Li, X. Ruan and H. Bao, *Physical Review B*, 2019, **100**, 144306.